Understanding the Origin of Oscillatory Phenomena Observed Between Wind Farms and HVDC Systems

Mohammad Amin, *Member, IEEE* and Marta Molinas, *Member, IEEE*

Abstract—Field experience has shown that sub-synchronous oscillation (SSO) and harmonic resonance can occur between wind farms (WFs) and high voltage dc (HVDC) systems. The oscillations can appear in the presence of background harmonics due to the interaction between the wind energy conversion system's (WECS) converter controller, HVDC converter controller and the impact of the interconnection system impedance. However, the root causes of these oscillations observed in the field are not entirely understood and they can be attributed to various sources within the components and controllers of the interconnected system. This paper explores the possible causes of these oscillations by investigating the impact of controllers and components in the wind farm and in the voltage source converter (VSC)-based HVDC transmission system. In order to understand this phenomena, the impedance of both the wind farm and the HVDC from the offshore ac collection point are analytically derived to identify potential resonance points. The impedance frequency responses of the wind farm and the HVDC converter indicate the potential resonance at low frequency. The origin of these oscillations can be attributed to the propagation of the WECS resonance through the WECS full converter dc link and the interaction between the WECS and the HVDC system. Once the source and the load impedance are identified, an impedance-based stability method is adopted in order to determine the stability. In an attempt to improve the oscillatory phenomena, an active damping scheme is implemented on the offshore HVDC rectifier. An analysis and time domain simulation results with its respective harmonic spectra show that the implemented active damping is very effective in eliminating the oscillations observed in the interconnected system. Moreover, this paper presents the role of the ratio between the bandwidths of the interconnected areas, as having an essential role in the root cause of the instability. The general rule is observed that when the bandwidth of the HVDC rectifier (which is the source) is faster than the bandwidth of the load (WFs inverter); the system operates stably.

Index Terms—High voltage dc (HVDC), Offshore grid, Stability Analysis, Harmonic Resonance, Subsynchronous Oscillation, Active damping, wind farm, Control of Voltage Source Converter (VSC).

I. Introduction

WITH rapid development of offshore wind power, the power rating of the offshore wind farm is becoming larger as the installation moves farther offshore and it thus, requires long transmission line to connect to the main ac grid [1]. High voltage dc (HVDC) transmission system is one feasible way to integrate the offshore wind power [2]- [5]. The HVDC system has been dominated by line commutated converters (LCC); however, voltage source converters (VSCs) which include two-level, multi-level [6] and modular multi-level converters [7], [8] are increasing dramatically due to having superior system performance and controllability [9].

The stability of the offshore wind power network connected through HVDC transmission line is a critical problem since there is no direct connection at ac collection (ACC) bus to a strong ac grid. Field experience has shown that sub-synchronous oscillation (SSO) and harmonic resonance can occur between wind farms and HVDC systems [10]. The oscillations can appear in the presence of background harmonics and is arguably resulting from the controller interaction of the wind energy conversion system (WECS) converter controller and HVDC converter controller [11]. These SSO and harmonic resonance phenomena are reported by many researchers and different mitigation techniques are proposed [12]- [20]. These analysis are mainly for the WECS connected directly to the main ac grid or connected to main ac grid through HVDC system where wind farms are represented by simple constant power source neglecting the control dynamics of the wind turbine drive train. However, the root cause of these oscillations observed in the field are not entirely understood and they can be attributed to various sources within the components and controllers of the interconnected system.

In this study, a full-scale type-four WECS is investigated which is connected to the main ac grid through two-level VSC-based HVDC system. The system is shown in Fig. 1. It has two wind farms which are connected to the ACC bus through offshore sea cable. The power is transferred to the grid through HVDC line. There is no rotating machine connected to ACC bus. The control architectures of the converters are as follows:

- The ACC bus side WECS converter regulates the dc voltage and reactive power of the WECS.
- The WECS generator side converter is a simple full bridge diode rectifier [21]. The speed of the generator is controlled by means of controlling the dc link current of the WECS. A dc-dc converter is used to regulate the dc link current of the WECS which inner control loop is the dc link current control and the outer control loop is a speed control of the wind turbine generator (WTG).
- The ACC bus side offshore HVDC converter is used to control the ac voltage. In this case, a inner loop current controller and a outer loop voltage controllers are also assumed. An active damping method is implemented for this converter.
- The ac grid side onshore HVDC converter regulates the dc link voltage and reactive power.

The authors are with the Department of Engineering Cybernetics, Norwegian University of Science and Technology, Trondheim-7491, Norway. (e-mail:mohammad.amin@ntnu.no; marta.molinas@ntnu.no).
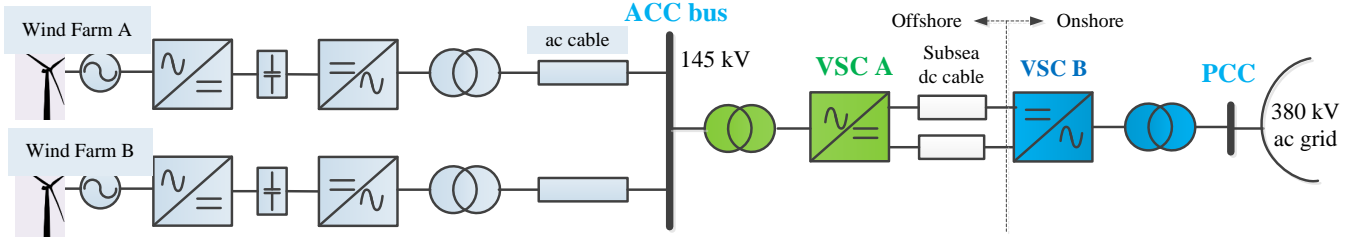
Fig. 1: Overview of the investigated system structure: VSC-based HVDC system for integration of wind farm.

The operation of the interconnected system is found to be poor without the closed loop ac voltage controller at ACC bus side converter of the HVDC system. The system performance is improved when a close-loop ac voltage control is used; however, an oscillatory phenomena around 15 Hz is observed when the closed loop ac voltage control is introduced due to interaction of the control dynamics and the impact of the impedance on the system dynamics. In order to understand this phenomena, the impedance of both the wind farm inverter and the HVDC rectifier from the offshore ac collection point are analytically derived and the impedance-based stability criteria, which is a simple method for analysis a complex power electronics based power system [22]- [27], is adopted to analyze the stability of the interconnected system. Once the source and the load impedance are analytically obtained, the impedance-based Generalized Nyquist Stability Criteria (GNC) is applied to predict the stability of the interconnected system [28]. The frequency domain impedance characteristics both for the wind farm and the HVDC rectifier from the offshore ACC point are presented to identify the potential resonance points. The Nyquist plots of the impedance ratio of the HVDC converter to the wind farm indicate the potential resonances at low frequency. An active damping scheme is implemented on the current compensator of the offshore HVDC rectifier in an attempt to improve the oscillatory phenomena. An analysis and time domain simulation results with its respective spectral analysis show that the implemented active damping is very effective in eliminating the oscillations observed in the interconnected system. The proposed active damping scheme can significantly reduce the magnitude of the source (HVDC rectifier) impedance at low frequencies which improves the stability of the interconnected system. Moreover, this paper is introducing a discussion of the role of the ratio between the bandwidths of the interconnected areas, as having an essential role in the root cause of instability and in being a strong factor to be taken into account in the shaping of the impedances to maintain stability.

The rest of the paper is organized as follows. Section II describes the modeling and control of the HVDC system which also includes the impedance modeling of the HVDC rectifier. Section III presents the modeling and control of the WECS. The stability analysis is presented in section IV. The section V presents the method of mitigating the SSO. A discussion is included in section VI. Finally the results of this study are concluded in Section VII.
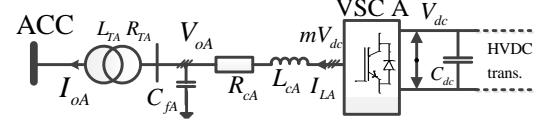

Fig. 2: The VSC-HVDC converter station

II. HVDC SYSTEM MODELING AND CONTROL

A. System Configuration

The HVDC system depicted in Fig. 1 consists of converter transformers, offshore HVDC rectifier (VSC-A), subsea dc cable and grid side onshore HVDC inverter (VSC-B). The VSC-HVDC system has a capacity of 200 MVA equivalent. The VSC-A behaves as a voltage source to the ac terminal and is connected to the ACC bus through a 145/200 kV, 50 Hz transformer with same rating as the converter. The VSC-B is connected to the main ac grid of 380 kV through a 200/380 kV, 50 Hz, 200 MVA transformer. The HVDC-link dc voltage is 400 kV and the length of the dc line is 200 km.

B. Analytical Modeling of VSC-HVDC

The electrical circuit of a VSC-HVDC converter for analytical modeling is shown in Fig. 2 where L_{cA} and R_{cA} are the total series inductance and resistance of the converter, C_{fA} is the filter capacitance, C_{dc} is the dc link capacitance and L_{TA} and R_{TA} are the equivalent series inductance and resistance of the transformer. The modeling, analysis and the control of the system will be presented in a synchronous reference frame (SRF). The transformation of the three phase quantity from stationary reference frame to SRF is based on the amplitude-invariant Park transformation, with the d-axis aligned with the voltage vector v_{oA} and q-axis leading the d-axis by 90^0. The dynamic equations of the converter in per unit (pu) can be given by [29], [30]

$$\begin{bmatrix} v_{odA} \\ v_{oqA} \end{bmatrix} = \begin{bmatrix} m_{dA} \\ m_{qA} \end{bmatrix} v_{dcA} - Z_{oA} \begin{bmatrix} i_{LdA} \\ i_{LqA} \end{bmatrix} \qquad (1)$$

where

$$Z_{oA} = \begin{bmatrix} R_{cA} + sL_{cA}/\omega_b & -\omega_1 L_{cA} \\ \omega_1 L_{cA} & R_{cA} + sL_{cA}/\omega_b \end{bmatrix};$$

ω_b is the base angular frequency; ω_1 is the fundamental angular frequency in pu; m_{dA} and m_{qA} are the d-axis and q-axis modulation index, respectively; the variable, s is used as the differential operator, s=d/dt, and the voltages and the
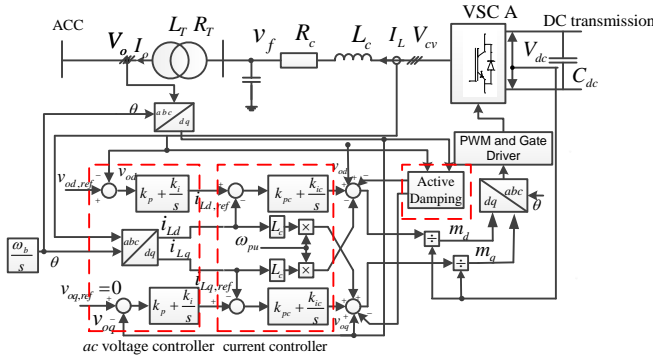
Fig. 3: Overview of the control structure of HVDC rectifier, VSC-A.

currents are indicated in Fig. 2. The subscript '$_A$' denotes the VSC-A.

C. Control of VSC-HVDC

The HVDC system converters have different control objectives depending on their location and system modeling. The point-to-point connection HVDC system used with the purpose of integrating wind farm must have the *dc* and *ac* voltage control objectives. The converter connected to the wind power side ACC bus regulates the ac voltage and supplies the sinusoidal voltage to the ACC bus and the other converter connected to the *ac* main grid regulates HVDC-link dc voltage and the reactive power. In this work, the focus is to study the interaction between the WECS and the ACC side HVDC converter, therefore the details of modeling, control and the impedance model will be presented only for the ACC side VSC HVDC assuming the *dc* voltage controller of VSC-B is providing constant dc voltage input to VSC-A.

The overview of the control structure of VSC-A is shown in Fig. 3. An outer-loop PI-controller is used to obtain the d-axis and q-axis current reference of VSC-A. A current controller is assumed to limit the current during abnormal operation. The reference current to the current controller, $i_{Ld,refA}$ and $i_{Lq,refA}$ can be defined by

$$\begin{bmatrix} i_{Ld,refA} \\ i_{Lq,refA} \end{bmatrix} = \overbrace{\begin{bmatrix} H_{vac}(s) & 0 \\ 0 & H_{vva}(s) \end{bmatrix}}^{G_{vA}} \left(\begin{bmatrix} v_{od,refA} \\ v_{oq,refA} \end{bmatrix} - \begin{bmatrix} v_{od} \\ v_{oq} \end{bmatrix} \right)$$

(2)

and PI-controller transfer function is

$$H_{vac}(s) = k_{pvac} + k_{ivac}/s \qquad (3)$$

where, $v_{od,refA}$ and $v_{oq,refA}$ are the reference d-axis and q-axis voltage, respectively; k_{pvac} and k_{ivac} are the proportional and integral gain of the PI-controller.

The inner-loop current-controller depicted in Fig. 3 is assumed to be the widely used SRF PI-controller of the VSC with decoupling term. The modulation index references obtained from the current controllers, including the feed-
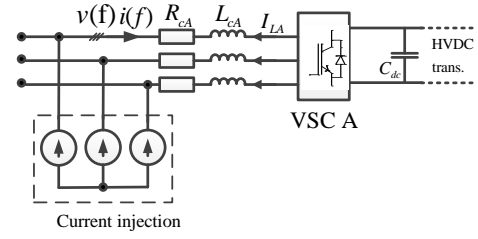

Fig. 4: The VSC's impedance verification setup based on shunt current injection

forward terms can be given by

$$\begin{bmatrix} m_{d.refA} \\ m_{q,refA} \end{bmatrix} = G_{ccA} \begin{bmatrix} i_{Ld,refA} \\ i_{Lq,refA} \end{bmatrix} + \begin{bmatrix} v_{odA} \\ v_{oqA} \end{bmatrix} - (G_{ccA} + G_{delA}) \begin{bmatrix} i_{LdA} \\ i_{LqA} \end{bmatrix}$$

(4)

where

$$G_{ccA} = \begin{bmatrix} H_{iA}(s) & 0 \\ 0 & H_{iA}(s) \end{bmatrix}$$

$$G_{delA} = \begin{bmatrix} 0 & \omega_1 L_{cA} \\ -\omega_1 L_{cA} & 0 \end{bmatrix}$$

and, $i_{Ld,refA}$ and $i_{Lq,refA}$ are the reference active and reactive current components obtained from the outer loop controller; the current compensator transfer function is $H_{iA} = k_{pcA} + k_{icA}/s$; k_{pcA} and k_{icA} are the proportional and integral gain of the current controller, respectively.

D. Impedance Modeling of VSC-A

In order to solve (1) for impedance in frequency domain, the modulating signal, m_{dqA} should be found as functions of i_{LdqA} and v_{odqA} in frequency domain. Applying linearization on (2) and (4) and after rearranging, the modulation index of VSC-A can be written as

$$\begin{bmatrix} \Delta m_{d.refA} \\ \Delta m_{q,refA} \end{bmatrix} = (I - G_{ccA}G_{vA}) \begin{bmatrix} \Delta v_{odA} \\ \Delta v_{oqA} \end{bmatrix} - (G_{ccA} + G_{delA}) \begin{bmatrix} \Delta i_{LdA} \\ \Delta i_{LqA} \end{bmatrix}.$$

(5)

Assuming the dc voltage controller performance of VSC-B is quite satisfactory and providing a constant dc voltage, therefore for simplification of analysis, it is reasonable to assume a constant dc voltage input to VSC-A. By doing this, we are ruling out any influence of Background harmonics coming from the on-shore grid.

Now after linearising (1) and inserting (5), gives the impedance model of the HVDC rectifier, VSC-A in dq-frame and can be given by

$$[Z_{dqA}]_{2x2} = -\frac{Z_{0A} + V_{dc0A}G_{PWM}(G_{ccA} + G_{delA})}{I - V_{dc0A}G_{PWM}(I - G_{ccA}G_{vA})} \quad (6)$$

where G_{PWM} is the PWM delay and can be modelled as $G_{PWM} = 1/(1 + 1.5sT_{sw})$ and $T_{sw} = 1/f_{sw}$; f_{sw} is the switching frequency; I is the 2x2 identity matrix and V_{dc0A} is the dc voltage at operating point.

Fig. 5: Comparison of Analytical model and the simulation for input impedance of HVDC Rectifier, VSC-A (solid line is analytical model and the circles are from the numerical simulation)

The impedance model derived analytically is verified by numerical simulation. The impedance model, $[Z_{dqA}]_{2x2}$ is derived in dq-domain which is 2x2 matrix. A perturbation current (5% of rated ac base current) at different frequencies is applied as shown in Fig. 4 and the voltage is measured. Fast Fourier Transformation (FFT) tool from SimPower System is used to analyze the different harmonic voltage and current. The impedance is calculated by dividing the voltage by current at each frequency. Since the frequencies are referred to the dq-frame, the perturbation is transformed back to the phase domain in order to be compatible with the injection structure as shown in Fig. 4. The current-controller is tuned based on the symmetrical optimum criteria [31] and is found to be $H_{iA}(s) = 0.6366 + 7.5/s$ in pu and the control loop bandwidth is 400 Hz with 90 degrees phase margin. The ac voltage controller proportional gain is kept 0.5 in pu with time constant of 12.5 ms for integral term and the control loop crossover frequency is 185 Hz with 60 degree phase margin. The analytical and simulation impedances are shown in Fig. 5 and the parameters used for this system are given Table II in Appendix. The solid line is representing the predicted impedances and the circles show the results from the numerical simulation. Both analytical and simulation impedances magnitude and phase are in good agreement. If we neglect the PWM delay, the off-diagonal terms of the dq-frame impedances become zero in analytically, since this converter does not have any PLL and the transformation angle for stationary abc to the dq is obtained from system fundamental frequency as $\theta_1 = \int^t 2\pi f_1 dt$ as shown in Fig. 3.

III. WIND ENERGY CONVERSION SYSTEM MODELING AND CONTROL

A. System Configuration

The investigated system shown in Fig. 1 has two wind farms which are connected to an ac collection point through a 25/145

Fig. 6: The wind turbine generator including full-scale converter and filter

Fig. 7: Overview of the control structure of Wind Power Inverter.

kV transformer and 10 km long undersea cable. The wind turbine generators (WTGs) are assumed to be a full-scale type-four WECS as depicted in Fig. 6. The detailed control of the wind turbine including the pitch regulator and generator speed regulator is presented in [32]. Each wind farm is assumed to have 28 turbines with 2 MW rating each. To simplify the system model, 28 turbines are lumped into one unit of 56 MW generation capacity.

B. Control of WECS

A full-scale converter system is utilized to transfer the energy produced by the wind turbine. In generator side, a full bridge diode rectifier is used which simplifies the converter control interaction. It transfers the energy produced by the wind generator to dc side. A two-level VSC converter is used in grid side. In between these two ac-dc converters, a dc-dc converter is used to regulate the speed of the WTG by controlling the dc link current of WECS.

The dynamic equation of WECS grid side VSC in pu can be given by

$$\begin{bmatrix} v_{odw} \\ v_{oqw} \end{bmatrix} = \begin{bmatrix} m_{dw} \\ m_{qw} \end{bmatrix} v_{dcw} - Z_{0w} \begin{bmatrix} i_{Ldw} \\ i_{Lqw} \end{bmatrix} \quad (7)$$

$$C_{dcw} \frac{dv_{dcw}}{dt} = I_0 - i_{dcw} \quad (8)$$

where

$$Z_{0w} = \begin{bmatrix} R_{cw} + sL_{cw}/\omega_b & -\omega_1 L_{cw} \\ \omega_1 L_{cw} & R_{cw} + sL_{cw}/\omega_b \end{bmatrix}.$$

The current controller as shown in Fig. 7 is assumed to be the widely used SRF PI controller of the VSC with decoupling

term. The modulation index references obtained from the current controllers can be given by

$$\begin{bmatrix} m_{d,refw} \\ m_{q,refw} \end{bmatrix} = G_{ccw} \begin{bmatrix} i_{Ld,refw} \\ i_{Lq,refw} \end{bmatrix} + \begin{bmatrix} v_{odw} \\ v_{oqw} \end{bmatrix}$$
$$- (G_{ccw} + G_{delw}) \begin{bmatrix} i_{Ldw} \\ i_{Lqw} \end{bmatrix} \quad (9)$$

and defined,

$$G_{ccw} = \begin{bmatrix} H_{iw}(s) & 0 \\ 0 & H_{iw}(s) \end{bmatrix}$$

$$G_{delw} = \begin{bmatrix} 0 & \omega_{PLL} L_{cw} \\ -\omega_{PLL} L_{cw} & 0 \end{bmatrix}$$

where $i_{Ld,refw}$ and $i_{Lq,refw}$ are the d- and q-axis current references, respectively; the current compensator transfer function is $H_{iw}(s) = k_{pcw} + k_{icw}/s$ where k_{pcw} and k_{icw} are the proportional and integral gain of the current controller, respectively and ω_{PLL} is the frequency of the PLL in pu.

A PI-controller is used in the outer-loop to control the dc-link voltage of WECS. The overview of the control structure is depicted in Fig. 7. The reference d-axis current to current controller, $i_{Ld,refw}$ is defined by

$$i_{Ld,refw} = H_{vdcw}(s)(v_{dc,refw} - v_{dcw})(-1) \quad (10)$$

and defined,

$$G_{dc} = \begin{bmatrix} H_{vdcw}(s) & 0 \\ 0 & 0 \end{bmatrix}$$

where, $v_{dc,refw}$ and v_{dcw} are the reference and measured dc voltage of WECS dc link, respectively; $H_{vdcw}(s) = k_{pvdc} + k_{ivdc}/s$ and k_{vdc} and k_{ivdc} are the proportional and integral gain of the dc voltage controller.

The phase locked loop (PLL) is used to track the frequency [33] which acts as a closed control loop. A second order PLL is assumed as shown in Fig. 8 and neglecting the dynamics of low pass filter, the instantaneous frequency deviation, $\delta\omega_{PLL}$ can be given by

$$\frac{d\delta\theta_{PLL}}{dt} = \delta\omega_{PLL} = H_{PLL}(s)v_{oqw}^{PLL} \quad (11)$$

and the angle difference,

$$\delta\theta_{PLL} = \theta_{PLL} - \theta_1 \quad (12)$$

where PI controller transfer function, $H_{PLL}(s) = k_{p,PLL} + k_{i,PLL}/s$ and $k_{p,PLL}$ and $k_{i,PLL}$ are the proportional and integral gain of the PLL, respectively; θ_{PLL} is the transformation angle of PLL and θ_1 is the transformation angle at fundamental frequency. The frequency of PLL, ω_{PLL} can be found by adding the nominal frequency, ω_1 with frequency deviation and is given by

$$\omega_{PLL} = \delta\omega_{PLL} + \omega_1 \quad (13)$$

and transformation angle can be found by

$$\frac{d\theta_{PLL}}{dt} = H_{PLL}(s)v_{oqw}^{PLL} + \omega_1. \quad (14)$$

The transformation from stationary reference to dq-frame can be described as $v_{ow,\alpha\beta}^s = e^{j\theta_1} v_{ow,dq}$ at grid frequency and
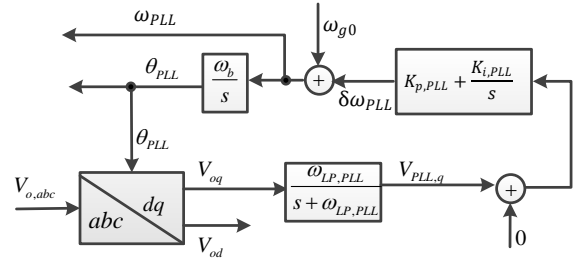
Fig. 8: Implemented Phase Locked Loop (PLL).

$v_{ow,\alpha\beta}^s = e^{j\theta_{PLL}} v_{ow,dq}^{PLL}$ at WECS converter PLL frequency. The relation between grid and converter dq-frame can be written by

$$v_{ow,dq}^{PLL} = e^{-j\delta\theta_{PLL}} v_{ow,dq}$$
$$= (cos(\delta\theta_{PLL}) - jsin(\delta\theta_{PLL}))(v_{od} + jv_{oq}) \quad (15)$$

and $\delta\theta_{PLL}$ is assumed to be very small which gives

$$v_{odw}^{PLL} + jv_{oqw}^{PLL} = (v_{odw} + v_{oqw}\delta\theta_{PLL})$$
$$+ j(v_{oqw} - v_{odw}\delta\theta_{PLL}). \quad (16)$$

Inserting this relation and applying Laplace transformation on (11), the PLL transfer function can be written by

$$\delta\theta_{PLL} = \overbrace{\frac{H_{PLL}(s)}{s + V_{od0w}H_{PLL}(s)}}^{G_{PLL}(s)} \Delta v_{oqw}. \quad (17)$$

The integral part of $H_{PLL}(s)$ is used to remove the quasi-steady-state phase error and it appears when synchronous frequency deviates from its nominal value. In steady-state, Δv_{oqw} is zero, $H_{PLL} = k_{p,PLL}$ is sufficient to keep $\delta\theta_{PLL}$ to zero. $G_{PLL}(s)$ is assumed to be a first order low pass filter. The bandwidth of PLL loop must be sufficiently small to reject the harmonic resonance [34]. By a rule, it should be 10 times less than the inner current control loop bandwidth, $\alpha_{cc} = k_{pc}/L_c$ [35].

C. Impedance Model of ACC side WECS VSC

In order to solve (7) for impedance in frequency domain, the modulating signal, m_{dqw} should be found as functions of i_{Ldqw} and v_{odqw} in frequency domain and also it is necessary to find the relation between ac and dc side. An ideal lossless model is assumed for the converter. Therefore power balance constraint between dc and ac side can be given by

$$i_{dcw}v_{dcw} = (i_{Ldw}m_{dw} + i_{Lqw}m_{qw})v_{dcw}. \quad (18)$$

Assuming the output power of WECS constant for a particular wind speed, therefore, it can be written as

$$\Delta P_{dcw} = 0 = I_{dc0w}\Delta v_{dc} + V_{dc0w}\Delta i_{dc}$$

and

$$R_{dcw} = \Delta v_{dcw}/\Delta i_{dcw} = -V_{dc0ww}/I_{dc0w}.$$

The relation between I_o and v_{dcw} including the dc-dc converter inductance can be written as

$$I_o = -\frac{1}{sL_{dcw} + R_{dcw}} v_{dcw} \quad (19)$$

Linearising (8), (18) and inserting (19), it can be written

$$\begin{bmatrix} \Delta v_{dcw} \\ 0 \end{bmatrix} = -G_{vi} \begin{bmatrix} i_{Ldw} \\ i_{Lqw} \end{bmatrix} - G_{vd} \begin{bmatrix} m_{dw} \\ m_{qw} \end{bmatrix} \qquad (20)$$

where

$$G_{vi} = \begin{bmatrix} Z_{dc}m_{d0w} & Z_{dcw}m_{q0w} \\ 0 & 0 \end{bmatrix};$$

$$G_{vd} = \begin{bmatrix} Z_{dcw}I_{Ld0w} & Z_{dcw}I_{Lq0w} \\ 0 & 0 \end{bmatrix};$$

$$Z_{dcw} = \frac{sL_{dcw} + R_{dcw}}{s^2 C_{dcw}L_{dcw} + sC_{dcw}R_{dcw} + 1}.$$

The modulation index references in (9) are in PLL reference. It is necessary to convert them into system reference. The voltage and current in system reference can be converted using transfer function of PLL derived in (17) and can be written as

$$\begin{bmatrix} \Delta i_d^c \\ \Delta i_q^c \end{bmatrix} = \begin{bmatrix} \Delta i_d^s \\ \Delta i_q^s \end{bmatrix} + \overbrace{\begin{bmatrix} 0 & G_{PLL}(s)I_q^s \\ 0 & -G_{PLL}(s)I_d^s \end{bmatrix}}^{G_{PLL}^i} \begin{bmatrix} \Delta v_d^s \\ \Delta v_q^s \end{bmatrix} \qquad (21)$$

$$\begin{bmatrix} \Delta v_d^c \\ \Delta v_q^c \end{bmatrix} = \overbrace{\begin{bmatrix} 1 & G_{PLL}(s)V_d^s \\ 0 & 1 - G_{PLL}(s)V_d^s \end{bmatrix}}^{G_{PLL}^v} \begin{bmatrix} \Delta v_d^s \\ \Delta v_q^s \end{bmatrix} \qquad (22)$$

and the modulation index in system reference can be given by

$$\begin{bmatrix} \Delta m_{dw} \\ \Delta m_{qw} \end{bmatrix} = G_A^{-1} \left(G_B \begin{bmatrix} \Delta i_{Ldw} \\ \Delta i_{Lqw} \end{bmatrix} + G_C \begin{bmatrix} \Delta v_{odw} \\ \Delta v_{oqw} \end{bmatrix} \right) \qquad (23)$$

where

$$G_A = (I + G_{pwm}G_{ccw}G_{dc}G_{vd})$$
$$G_B = G_{pwm} \left(-G_{ccw} + G_{delw} - G_{ccw}G_{dc}G_{vi} \right)$$
$$G_C = G_{pwm}((-G_{ccw} + G_{delw}) G_{PLL}^i + G_{PLL}^v$$
$$\qquad - G_{ccw}G_{dc}G_{vq})$$

and define the modulation index at operating point

$$G_D = \begin{bmatrix} m_{d0w} & 0 \\ m_{q0w} & 0 \end{bmatrix}.$$

Now applying linearization on (7) and substituting (20) and (23), gives the impedance model of ACC side WECS VSC in frequency domain as

$$[Z_{dqw}]_{2x2} = \frac{-Z_0 + V_{dc0w}G_A^{-1}G_B - G_D G_{vi} - G_D G_{vd}G_A^{-1}G_B}{I - V_{dc0w}G_A^{-1}G_C + G_D G_{vd}G_A^{-1}G_C}. \qquad (24)$$

The impedance model, $[Z_{dqw}]_{2x2}$ is derived in dq-domain which is a 2x2 matrix. This model is verified by numerical simulation. Same small-signal perturbation method as HVDC rectifier is applied to validate the impedance model. The analytical and simulation impedance is shown in Fig. 9 and the parameters for the controller and electrical circuit is given in Table III in Appendix. The solid line is representing the predicted impedance and the one with circles is from the numerical simulation. Both analytical and simulation impedance magnitude and phase are in good agreement. In the analytical
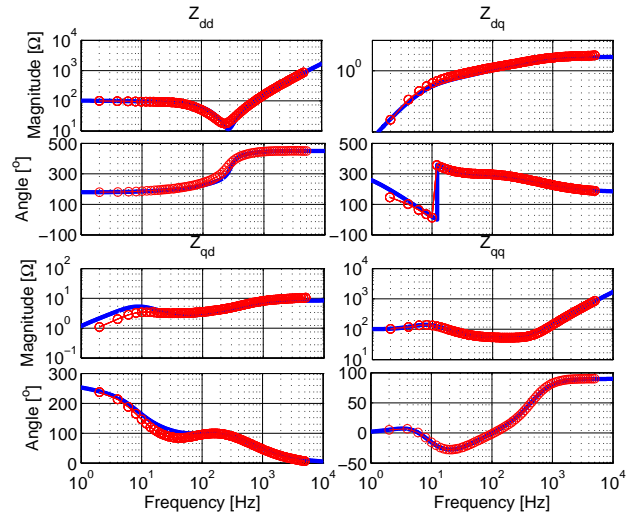

Fig. 9: Impedance model verification of ACC side WECS VSC for dc voltage control (solid line is analytical model and the circles are from numerical simulation)

model the delay caused by sampling and the anti-aliasing filter is neglected which cause a little deviation in simulation in the off-diagonal elements.

IV. STABILITY ANALYSIS AND SIMULATION RESULTS

A. Impedance-Based Stability Analysis

The small-signal impedance model of interconnected system is shown in Fig. 10 where $Z_{HVDC,ACC}$ and $Z_{W,ACC}$ are total impedance of VSC-A and wind turbine from the offshore ACC point, respectively. The subscript for the dq has been dropped in the equivalent circuit. $Z_{HVDC,ACC}$ in (25) is found together with the parallel connection of HVDC inverter output filter impedance and series connection of transformer impedance.

$$Z_{HVDC,ACC,dq} = Z_{T,dq} + \left(Z_{dqA}^{-1} + Z_{Cf,dq}^{-1} \right)^{-1} \qquad (25)$$

In abc frame the transformer impedance is

$$Z_{T,abc} = \begin{bmatrix} R_T + sL_T & 0 & 0 \\ 0 & R_T + sL_T & 0 \\ 0 & 0 & R_T + sL_T \end{bmatrix} \qquad (26)$$

and the filter impedance is

$$Z_{Cf,abc} = \begin{bmatrix} sC_f & 0 & 0 \\ 0 & sC_f & 0 \\ 0 & 0 & sC_f \end{bmatrix}^{-1}. \qquad (27)$$
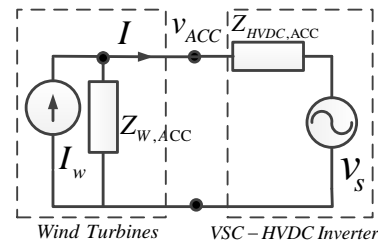

Fig. 10: Impedance based equivalent model of offshore ac grid system

The impedance model of the converter is derived in dq domain, therefore it is necessary to convert the abc frame impedance into $d - q$ frame impedance which can be given by

$$Z_{T,dq} = \begin{bmatrix} R_T + sL_T & -\omega_1 L_T \\ \omega_1 L_T & R_T + sL_T \end{bmatrix} \quad (28)$$

$$Z_{Cf,dq} = \begin{bmatrix} sC_f & -\omega_1 C_f \\ \omega_1 C_f & sC_f \end{bmatrix}^{-1}. \quad (29)$$

$Z_{W,ACC}$ in (30) is the impedance of the wind farm including impedance of the wind inverter output filter, transformer leakage inductance and the ac cable impedance, where n is the number of wind farms connected in parallel. The wind farms are identical in structure and control, and two wind farms are connected to the ACC bus, hence n=2.

$$Z_{W,ACC,dq} = \frac{1}{n} \left(Z_{cable} + Z_{T,dq} + \left(Z_{dqw}^{-1} + Z_{Cf,dq}^{-1} \right)^{-1} \right) \quad (30)$$

However, if the output power of the wind farms differs from each other, it is necessary to calculate the impedance of the wind power inverter separately for individual operating point and the total impedance of the wind farms can be calculated based on the parallel connection rule.

Based on this representation in Fig. 10, the response of the ACC bus voltage can be written as

$$V_{ACC,dq}(s) = (V_{s,dq}(s) + Z_{HVDC,ACC,dq}(s)I_{dq}(s))$$
$$\left(I + \frac{Z_{HVDC,ACC,dq}(s)}{Z_{W,ACC,dq}(s)} \right)^{-1}. \quad (31)$$

For system stability studies, it is assumed that

1) The ac voltage of VSC-A is always stable when unloaded; and
2) The WECS current is stable when it is connected to stable source.

Therefore, the stability of the interconnected system depends on the second term of right-hand side of (31) and the ACC bus voltage will be stable if and only if the impedance ratio, $Z_{HVDC,ACC,dq}/Z_{W,ACC,dq}$ which can be defined as the minor loop gain of feedback control system as

$$G(s)H(s) = \frac{Z_{HVDC,ACC,dq}(s)}{Z_{W,ACC,dq}(s)} \quad (32)$$

meets the Generalized Nyquist Stability Criterion (GNC) [22]-[28].

The impedance ratio in dq-domain is a 2x2 matrix, hence multi-variable Nyquist stability criteria need to be applied to determine the stability of the interconnected system. The off-diagonal elements have an important role on the stability [36], [37]; however, their impact can be neglected in some cases, for example, in the case when the converter operates in unity power factor mode [38], [39], the matrix of the minor loop gain, $(Z_{HVDC,ACC,dq}Z_{W,ACC,dq}^{-1})$ is diagonally dominant [40]. The diagonal elements of the HVDC rectifier impedance are 10 times higher than the off-diagonal elements, and are diagonal dominant, shown in Fig. 5. The reactive power reference of the wind power inverter is zero, which
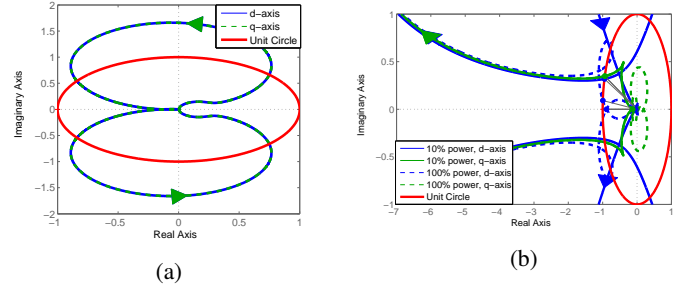

Fig. 11: Nyquist plot of impedance ratio: (a) the HVDC rectifier connected with CPL and (b) the wind farms connected with an ideal grid.

means, the wind power inverter is operating in unity power factor mode. Moreover, diagonal elements of the wind farm impedance seen from ac collection bus are 10 dB higher than the off-diagonal elements and are diagonally dominant. Since, the matrix, $(Z_{HVDC,ACC,dq}Z_{W,ACC,dq}^{-1})$ is diagonally dominant over entire Nyquist path, the stability of the interconnected system can be determined by the d-axis and q-axis impedance ratios and the off-diagonal elements can be ignored.

B. Stability of HVDC System with No-Load and CPL

The first assumption is trivial and minimum requirements for a HVDC transmission system installed in the purpose of integrating wind farms [11] and it has been verified for two cases, case 1: with no load condition and case 2: by connecting a constant power load (CPL). The power of the CPL is equivalent to the power of the wind farms. Note that the wind farms have been disconnected. The stability analysis has been performed by checking the Nyquist plot of the impedance ratio where the CPL load is simulated as $Z_{W,ACC,dq}$ and the Nyquist plot is shown in Fig. 11 (a). Since, the Nyquist plots do not encircle the point (-1, j0), the HVDC system operates stably which is further confirmed in time domain simulation. There is no oscillation in both the ac side and the dc side of the HVDC rectifier. The input dc voltage of HVDC rectifier is constant; therefore, for simplification of analytical analysis, it is reasonable to replace the onshore dc voltage controlled HVDC inverter by a dc voltage source and the onshore HVDC inverter controllers do not affect the analysis. However, if the HVDC system is unstable (for example oscillatory behaviour in the dc link voltage) before connecting to the wind farms, then it will be a stability problem of the HVDC system itself and it will not be an interaction phenomena of the controllers of the wind farm inverter and the HVDC rectifier.

C. Stability of Wind Farm with Ideal Grid

The wind turbine model has a drive train based on 2-masse model, a pitch control and a speed regulator which can introduce oscillation if they are not properly designed. Hence, the second assumption must be verified. In this paper, this assumption is verified by frequency domain analysis and also by numerical simulation. To identify if there is any oscillation
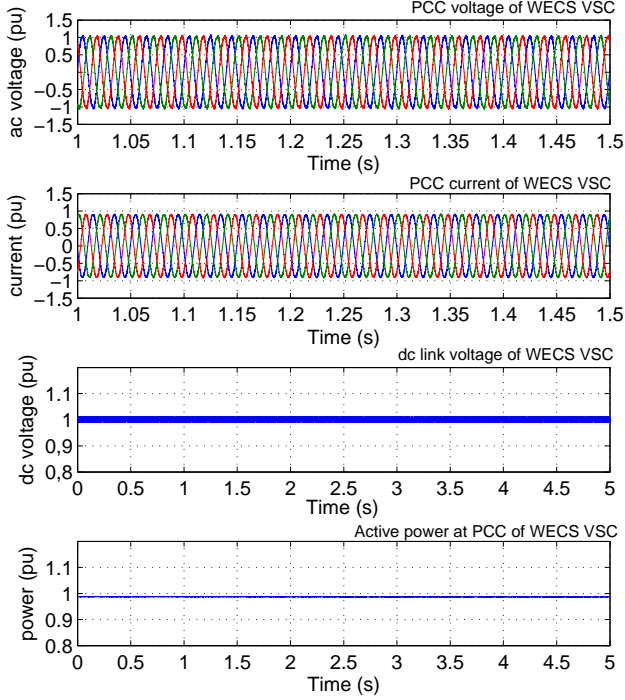
Fig. 12: The PCC voltages and currents of WECS, the dc link voltage of WECS and the PCC active power of WECS when it is connected to an ideal ac grid
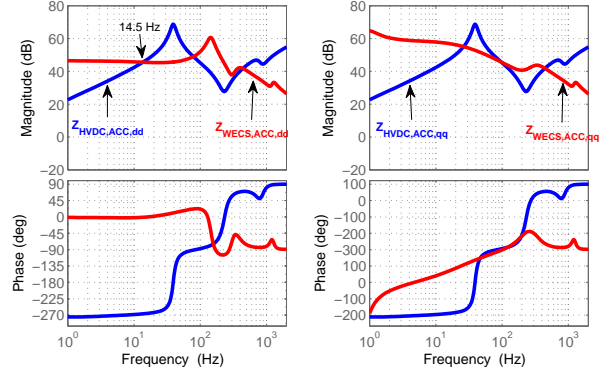

Fig. 13: The d-axis and q-axis impedance of the HVDC converter, $Z_{HVDC,ACC,dq}$ and the wind power inverter, $Z_{W,ACC,dq}$ seen from ACC bus. (Left-side Fig. is the d-axis impedance and the right-side Fig. is the q-axis impedance.)
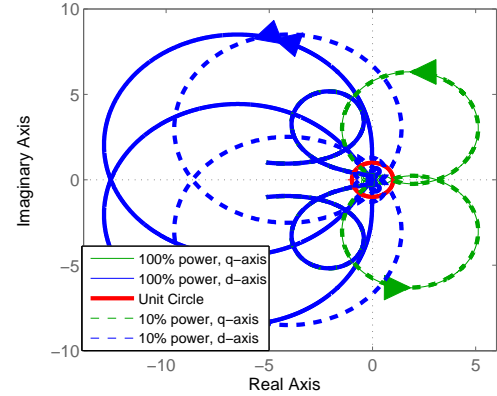

Fig. 14: Nyquist plot of impedance ratio for 10% and 100% wind power output (Blue-line is for the d-axis impedance ratio; green-line is for the q-axis impedance ratio and red-line is the unit circle.)

coming from the wind power inverters, the wind farms have been connected to an ideal grid instead of the HVDC system. Fig. 11 (b) shows the Nyquist plot of the impedance ratio for 10% and 100% wind power output where the HVDC system impedance is simulated by an ideal grid. The phase margin of the Nyquist plot of the d-axis impedance ratio is becoming smaller for the high wind power output meaning that the stability margin is reduced, while the q-axis impedance remains the same, since the q-axis impedance does not depend on the active power [23]. Moreover, if the grid strength is reduced by increasing the grid impedance, the phase margin of the Nyquist plot becomes smaller which decreases the stability margin of the system. The high output power causes high output current which increases the losses and reactive power consumption in the system and can provoke the instability.

Fig. 12 shows the PCC voltages and currents of the WECS VSC, the WECS dc link voltage and the active power at PCC of the WECS inverter. The wind farms system operates stably and there is no oscillation either in the ac side or in the dc link of the WECS which has confirmed that there is no intrinsic oscillation coming from the wind farms. As can be seen in Fig. 12, the wind power output is constant; therefore, the turbine mechanical control including the generator and the diode rectifier and the dc-dc converter can be replaced by a constant power source in the analytical formulations; hence these assumptions on the generator side converter and the dc-dc converter do not affect the results of the analysis. However, if the wind farms become unstable in ideal grid

connected mode, then the cause of the oscillation will not be an interaction problem of the wind farm inverter and the HVDC rectifier. It will be a stability problem of the wind farm itself.

D. Stability of HVDC System with Wind Farm

Now the wind farms have been connected to the HVDC system. Fig. 13 shows the d-axis and q-axis impedance of the HVDC rectifier, $Z_{HVDC,ACC,dq}$ and the wind power inverter, $Z_{W,ACC,dq}$ seen from the ACC bus. As can be seen, both the d- and q-axis impedance of the HVDC rectifier are equal, since the HVDC rectifier does not have any PLL and there is no coupling term in the converter itself. The first resonance point in the HVDC rectifier impedance is resulting from the integral term of the PI inner loop current control and the outer loop ac voltage controller and the second resonance is because of the LCL-filter. Similarly, the wind turbine inverter has a low frequency resonance point in the d-axis resulting from the cascaded dc voltage and current control; however in the q-axis

there is no outer control, thus there is no resonant point similar to the d-axis impedance at low frequency. The next resonance is from the LCL-filter. The wind power inverter has also some other resonances at high frequency which are caused by the ac cable.

Fig. 14 shows the Nyquist plot of the impedance ratio $Z_{HVDC,ACC,dq}/Z_{W,ACC,dq}$ for the d- and q-axis when the wind farms produce 10% and 100% of rated power. As can be seen, the q-axis impedance ratio satisfies the GNC, it doesn't encircles the point (-1, j0), which means that the interconnected system is stable for the q-axis input impedance ratio; however, the d-axis input impedance ratio encircles the point (-1, j0) regardless of the power level. Therefore, the interconnected system is unstable for d-axis impedance ratio. As can be seen from the d-axis Nyquist plot as shown in Fig. 14, the impedance ratio intersects the unit circle several times. The first intersecting point is at around 14.5 Hz as shown in the d-axis impedance in Fig. 13; therefore the system has one of the unstable eigenvalue with 14.5 Hz frequency and will have oscillatory behaviour at around 14.5 Hz which is caused by the resonance point introduced by the cascaded control loop of the HVDC rectifier and the wind power inverter. The q-axis HVDC impedance intersects the wind power inverter impedance several times as shown in Fig. 13; however the system is predicted to be stable by the GNC plot for the q-axis impedance as shown in Fig. 14. As can be seen in Fig. 14, the system is unstable regardless of the power levels and it indicates that the instability phenomena is caused by the controller interaction and not because of the power (energy) flow. There is no change in the Nyquist plot of the q-axis impedance, since q-axis impedances do not depend on the active power flow [23].

At 50 Hz base, the bandwidth of the current control loop of the wind power inverter is assumed to be less than (0.2x2kHz/50=) 8 pu. Applying modulus optimum criteria, the current controller is tuned at $H_{iw}(s) = 0.573 + 3.6/s$ in pu and the control-loop crossover frequency is 200 Hz with 90 degree phase margin [31]. Since the current control loop is modelled as a low pass-filter and the high frequency is removed by the high pass-filter, the frequency around 14.5 Hz predicted in impedance characteristics has significant impact on the system stability. The PLL PI controller transfer function is $H_{PLL}(s) = 0.0844 + 4.6908/s$ in pu and the control loop bandwidth is 9 Hz. The system is unstable predicted by GNC even the bandwidth of the PLL of the wind power inverter is sufficient low to reject the low frequency.

To validate the small-signal analysis above, a detailed time domain simulation model of the interconnected system as depicted in Fig. 1 has been built with detailed switching model of the VSC and the drive train of the WTG in the Matlab/Simulink environment associated with the SimPower-System Blockset. Fig. 15 (a) shows the resulting 3-phase ac voltages and currents at ACC bus from time domain response. The spectrum from FFT of them are also shown in Fig. 15 (a). It can be seen from the FFT both the voltages and currents at ACC bus have low frequency oscillation at around 35 Hz and 65 Hz. As predicted from the d-axis Nyquist plot of impedance ratio, there is a low frequency oscillation at 15 Hz which is
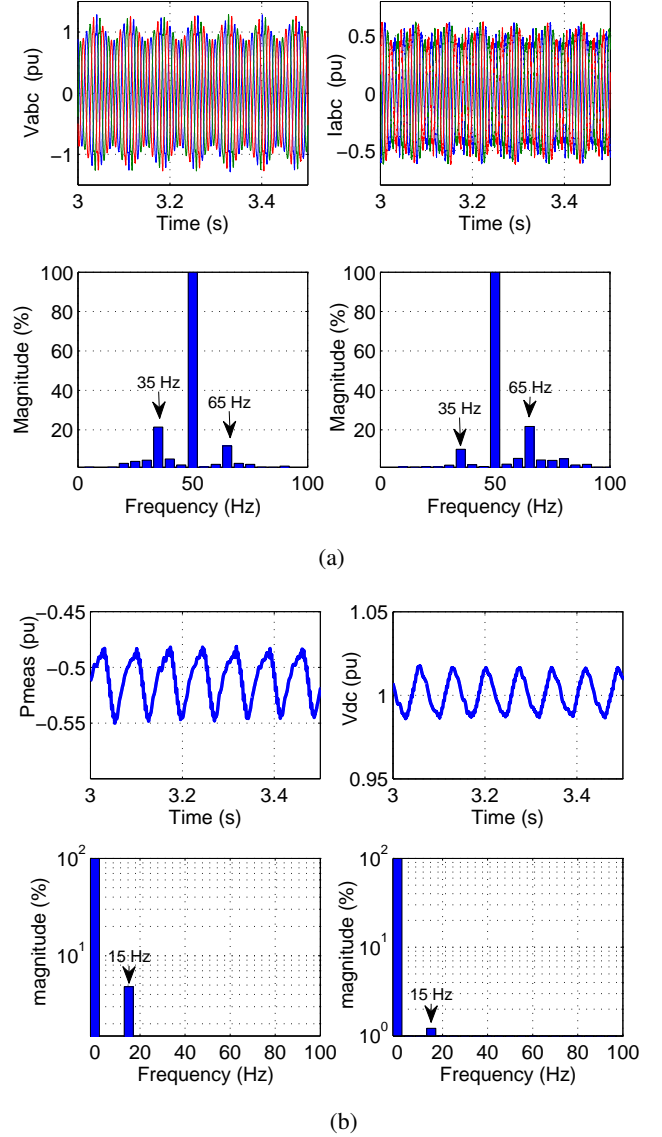

Fig. 15: Offshore side: (a) The 3-phase instantaneous voltages and currents at offshore ACC and FFT of them and (b) Active power at offshore ACC of VSC-A, dc voltage of HVDC system and FFT of them.

transformed into abc-frame as $\pm(f - f_1)$ [17]. The active power measured at the offshore ACC bus, the HVDC link dc voltage and FFT of them are shown in Fig. 15 (b). Both the active power at ACC and the dc link voltage of HVDC system are the dc quantity and have a SSO at around 15 Hz as predicted from the impedance model. This oscillation is noticed both for $H_{PLL}(s) = 0.0844 + 4.6908/s$ and $H_{PLL}(s) = 0.0844 + 0.0/s$ and results from the interaction between the HVDC rectifier and the wind power inverter.

This oscillation is moving towards the main ac grid through the HVDC link. The 3-phase instantaneous voltages and currents, FFT of current, the measured active power and the FFT of the active power at the onshore PCC of VSC-B are shown in Fig. 16. No ac voltage oscillation is noticed at the onshore PCC of the VSC-B, since it is connected to a strong ac

TABLE I: The source and the load bandwidth, the bandwidth ratio and the stability from the GNC.

Case number	Source Bandwidth (HVDC Rectifier) BW_s	Load Bandwidth (WFs inverter) BW_L	Bandwidth Ratio BW_s/BW_L	Generalized Nyquist Stability Criterion
1	185 Hz	200 Hz	0.925 (<1)	Encircles (-1, j 0) [Fig. 14]
2	315 Hz	200 Hz	1.575 (>1)	Does not encircle (-1, j 0) [Fig. 17]
3	336 Hz	200 Hz	1.680 (>1)	Does not encircle (-1, j 0)
4	185 Hz	100 Hz	1.850 (>1)	Does not encircle (-1, j 0)
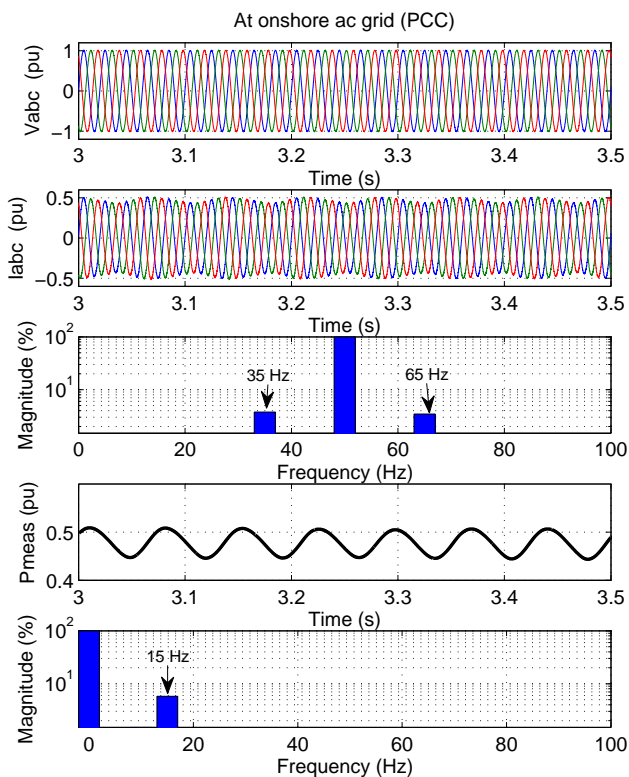
Fig. 16: Onshore side: The 3-phase instantaneous voltages and currents at PCC, FFT of current, measured active power and FFT of active power at onshore PCC of VSC-B.

Fig. 17: Nyquist plot of impedance ratio for 315 Hz bandwidth of ac voltage control loop of HVDC rectifier for 10% and 100% wind power output.

grid; however same frequency of oscillation in the current and the power are identified. This oscillation is propagating from the wind power inverter and the HVDC system as observed in Fig. 15.

V. PROPOSED MITIGATION TECHNIQUE

A. Modified Control Bandwidth

The impedance of both the HVDC rectifier and the wind power inverter can be reshaped by modifying the bandwidth of the controllers. Thus, the impact of the control bandwidth of the HVDC rectifier and the wind farms (WFs) inverter on the stability is discussed below.

1) Impact of the Current Control Loop Bandwidth of the HVDC Rectifier: Fig. 17 shows the Nyquist plot of the impedance ratio for a modified bandwidth of the HVDC

rectifier controller as an example case where the current controller is tuned at $H_{iA} = 1.2366 + 7.5/s$ in pu and the control loop bandwidth is 773 Hz with 90 degree phase margin while the original bandwidth was 400 Hz. For this current control tuning, the bandwidth of the ac voltage control loop (which is the source) becomes 315 Hz with 65 degree phase margin and the bandwidth ratio of the source to the load (WFs inverter) becomes greater than 1 (case 2 in Table I) while the original bandwidth ratio was less than 1 case 1 in Table I). As can be seen in Fig. 17, the Nyquist plots do not encircle the point (-1, j0); hence the system is stable which is further confirmed by numerical simulation.

2) Impact of the ac Voltage Control Loop Bandwidth of the HVDC Rectifier: An example case has been shown for increased bandwidth of the source (the ac voltage control loop of the HVDC rectifier) while the current control-loop bandwidth remains the same. The source bandwidth is increased by increasing the proportional gain of the ac voltage controller to $H_{vac} = 0.75 + 40/s$. The crossover frequency becomes 336 Hz with 50 degree phase margin and the bandwidth ratio of the source to the load becomes greater than 1 (case 3 in Table I). The interconnected system operates stably which is confirmed by checking the GNC plot and by numerical simulation.

3) Impact of the Current Control Loop Bandwidth of the WFs Inverter: Another example case is shown for a decreased bandwidth of the wind power inverter to 100 Hz with 90 degree phase margin while the source bandwidth remains the
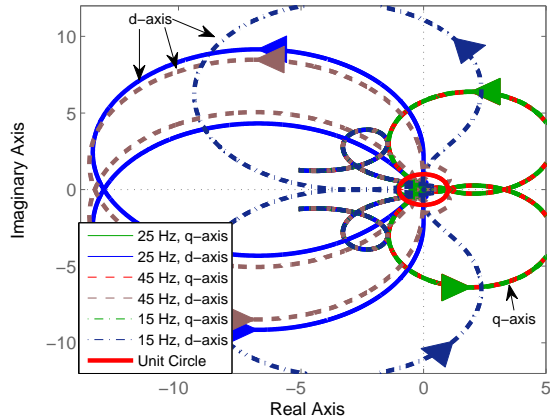
Fig. 18: Nyquist plot of impedance ratio for different bandwidth of the wind power inverter's dc voltage control loop.

same. For this tuning, the bandwidth ratio becomes larger than 1 (case 4 in Table I) and the interconnection becomes stable which is confirmed by the GNC and in the numerical simulation.

4) Impact of the dc Voltage Control Loop Bandwidth of the WFs Inverter: Since the oscillation frequency is around 15 Hz, which is similar to the control loop bandwidth of the PLL and dc link voltage control, their participation in the oscillation have been investigated. First we have checked the impact of the dc voltage control loop bandwidth on the stability. Initially, the dc voltage controller is tuned with a crossover frequency of 25 Hz and 160 degree phase margin and we observed the 15 Hz oscillation in the interconnection. Fig. 18 shows the Nyquist plots for different bandwidth of the wind power inverters dc voltage control loop. It has been observed that the higher bandwidth of the dc voltage control loop the more unstable the system becomes, while lower bandwidth makes the system stable but degrades the system performance significantly which is not desirable. The bandwidth of the dc voltage control loop has no impact on the q-axis impedance as shown in Fig. 18. The interconnected system remains unstable for different bandwidth of the dc voltage control loop of the wind power inverter.

5) Impact of the PLL Loop Bandwidth of the WFs Inverter: The interconnected system has now been investigated for different bandwidths of the PLL. The initial bandwidth of the PLL is 9 Hz with 46 degree phase margin for which 15 Hz oscillation has been observed. Fig. 19 (a) shows the PLL loop gain and Fig. 19 (b) shows the Nyquist plot of the impedance ratio for 0.1 Hz, 9.25 Hz and 15.5 Hz PLL bandwidth for the tuning of case 1 in Table I. As can be seen in Fig. 19 (a), the PLL loop gains are stable with sufficient phase margin; however the interconnected system is unstable for the d-axis minor loop gain from Fig. 19 (b). The PLL bandwidth has an impact only on the q-axis impedance [23]; therefore the phase margin of the q-axis Nyquist plot is reducing for higher bandwidths of the PLL. On the other hand, the d-axis impedance remains the same for a change of the PLL bandwidth. Thus, the PLL is not participating in the observed
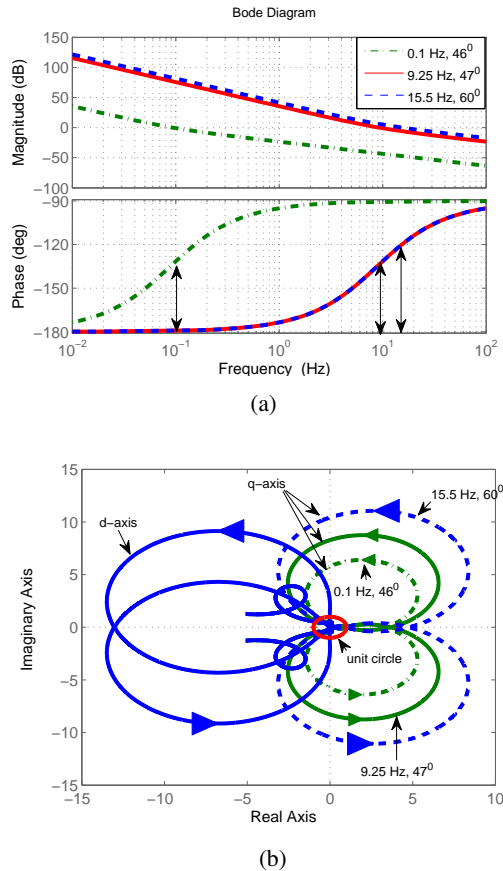

(a)

(b)

Fig. 19: (a) Wind power inverter's PLL loop gain for different PLL bandwidths and (b) Nyquist plot of impedance ratio for different bandwidth of the PLL for the controller bandwidth of case 1 of the Table I

oscillation, since the system is predicted to be unstable only for the d-axis Nyquist plot.

Table I shows the source and the load bandwidth, the bandwidth ratio and the stability from the bandwidth ratio of the interconnected system. From the above test we have found that the interconnected system operates stably as long as the loop bandwidth ratio of the source to the load becomes larger than 1. The ratio between the bandwidths of the interconnected areas has an essential role in the root cause of instability and is a strong factor to be taken into account in the shaping of the impedances to maintain stability. The control loop bandwidth is limited by the switching frequency of the VSC; therefore it is not reasonable to increase the bandwidth of the control loop, and on the other hand the slower bandwidth decreases the system performance. Alternately, an active damping scheme in the current compensator of the HVDC rectifier can be used to remove the SSO. The detailed modeling and analysis of the proposed active damping scheme is described below.

B. Active Damping Scheme

The phase voltage at ACC bus including the oscillatory components at different frequency in time domain can be
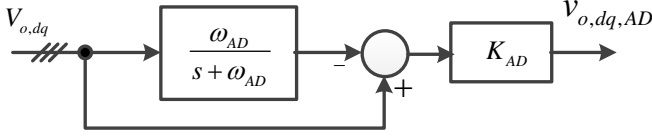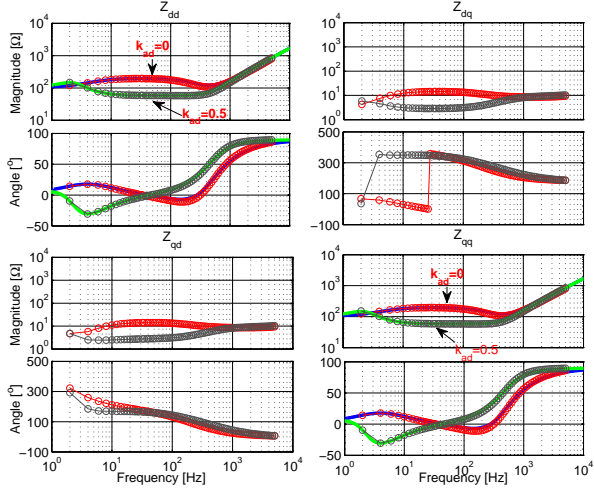
Fig. 20: Implemented active damping scheme

Fig. 21: Comparison of input impedance of HVDC rectifier, VSC-A with ($k_{ad} = 0.5$) and without ($k_{ad} = 0.0$) active damping. (Solid line is analytical model and the circles are from numerical simulation)

written as

$$v_{abc}(t) = V\cos(2\pi f_1 t + \theta) + \sum V_f \cos(2\pi f_f t + \phi_f) \quad (33)$$

where V corresponds to the magnitude of fundamental voltage at frequency f_1; θ is phase angle of 3 phase voltage (0, $2\pi/3$, $4\pi/3$) and V_f corresponds to the magnitude of voltages at different frequency f_f with phase ϕ_f. In frequency domain, it can be written by (34) where $V_1 = (V/2)e^{\pm j\theta}$ and others follow the similar notation and in dq-domain it can be represented by (35) [17].

$$V_a[f] = \begin{cases} V_1 & f = \pm f_1 \\ \sum V_f & f = \pm f_f \end{cases} \quad (34)$$

$$V_{od}[f] = \begin{cases} V\cos(\theta) & dc \\ \sum V_f[f] & f = \pm(f_f - f_1) \end{cases} \quad (35a)$$

$$V_{oq}[f] = \sum \mp j V_f[f] \quad f = \pm(f_f - f_1) \quad (35b)$$

The active damping is designed to suppress the oscillating term from (35). The active damping is, based on injecting a voltage component of counter phase with detected oscillation in order to produce a cancellation effect, done with VSC-A adding the modulating signal to the reference voltage in (4). The oscillation is first isolated by high pass filtering and is then multiplied by a gain K_{AD}. The high pass filter function is implemented by subtracting from measure voltage signals
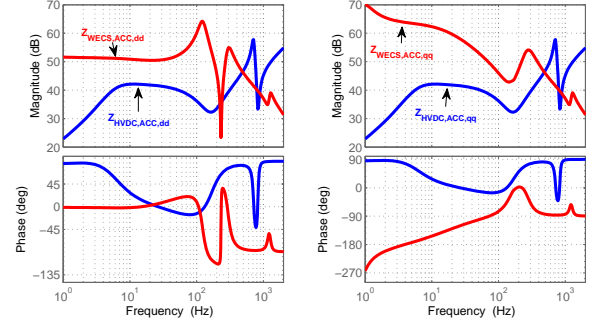
Fig. 22: The d-axis and q-axis impedance of HVDC converter, $Z_{HVDC,ACC,dq}$ and wind power inverter, $Z_{W,ACC,dq}$ seen from ACC bus including active damping term

a low pass filtered version of same voltages as shown in Fig. 20. The damping voltage reference is given by (36)

$$v_{o,dq,AD} = K_{AD}\left(-\frac{\omega_{AD}}{s + \omega_{AD}}v_{o,dq} + v_{o,dq}\right) = \rho_{AD}v_{o,dq} \quad (36)$$

where

$$\rho_{AD} = \frac{K_{AD}s}{s + \omega_{AD}}$$

and ω_{AD} is the cut-off frequency of the applied low-pass filter. Including the active damping term, the modulation index references of (4) from the current controller can be written as follows:

$$\begin{bmatrix} m_{cvd.refA} \\ m_{cvq,refA} \end{bmatrix} = G_{ccA}\begin{bmatrix} i_{Ld,refA} \\ i_{Lq,refA} \end{bmatrix} + G_{AD}\begin{bmatrix} v_{odA} \\ v_{oqA} \end{bmatrix}$$
$$- (G_{ccA} + G_{delA})\begin{bmatrix} i_{LdA} \\ i_{LqA} \end{bmatrix} \quad (37)$$

and

$$G_{AD} = \begin{bmatrix} 1 - \rho_{AD} & 0 \\ 0 & 1 - \rho_{AD} \end{bmatrix}.$$

The impedance based stability analysis is adopted again to analyze the stability of the system with the proposed damping scheme. The impedance model derived in (6) for HVDC converter VSC-A is modified to include the damping term and is given by

$$[Z_{dqA}]_{2x2} = -\frac{Z_0 + V_{dc0}G_{PWM}(G_{cc} + G_{del})}{I - V_{dc0}G_{PWM}(G_{AD} - G_{cc}G_v)}. \quad (38)$$

The impedance model derived analytically is verified by numerical simulation and the result is compared with the impedance model derived in (6) for the case without the damping term. Fig. 21 shows the input impedance model verification of HVDC rectifier where $k_{ad} = 0$ means that the active damping term is disabled and $k_{ad} = 0.5$ means that the active damping term is enabled with a damping gain of 0.5. The cut-off frequency of the low-pass filter is set to 3.18 Hz. As can be seen, the propose active damping can significantly reduce the magnitude of the input impedance of HVDC rectifier which means that it reduces the source impedance in (31) and extends the stability margin by increasing both phase-margin and gain-margin in GNC of the interconnected system.
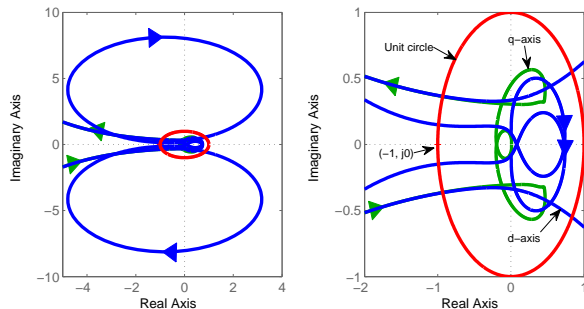
Fig. 23: Nyquist plot of impedance ratio with active damping gain of 0.5 (Left Fig. is full view and right figure is zoom view)
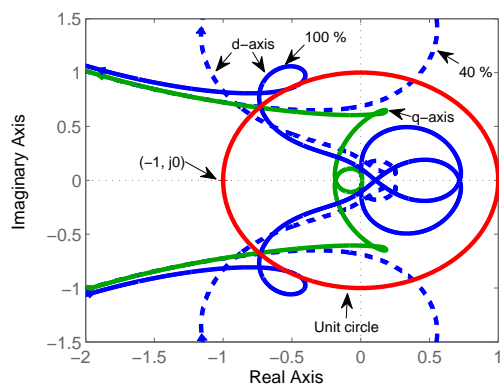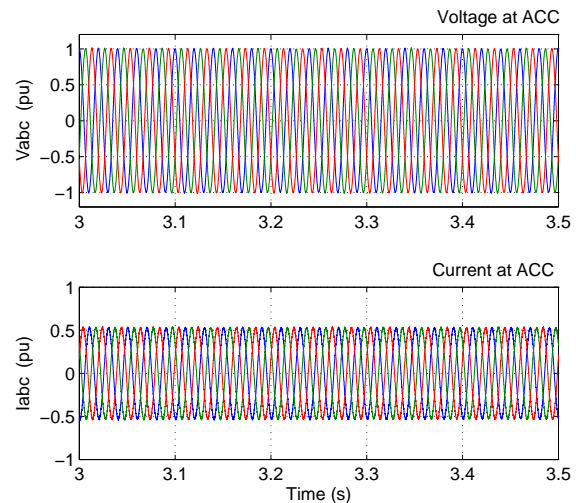

Fig. 24: Nyquist plot of impedance ratio with active damping gain of 0.5 for different wind power loading
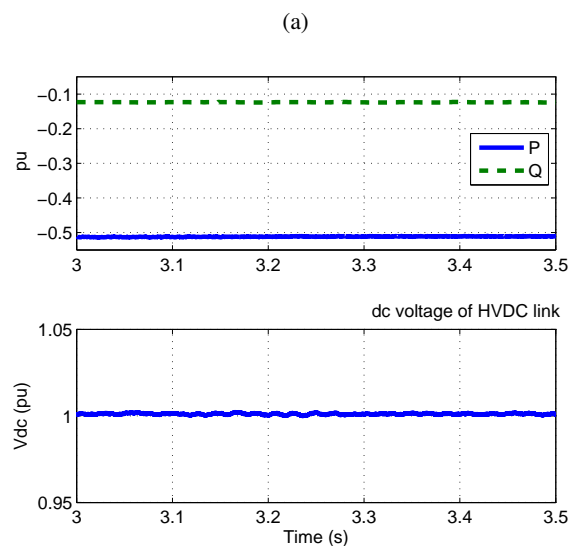

(a)

(b)

Fig. 25: Simulation results with active damping: (a) The 3-phase ac voltages and currents at ACC bus and (b) the active and reactive power at ACC of HVDC rectifier, VSC A and dc link voltage of HVDC system.

Fig. 22 shows the d-axis and q-axis impedance of the HVDC rectifier, $Z_{HVDC,ACC,dq}$ and the wind power inverter, $Z_{W,ACC,dq}$ seen from ACC bus including the active damping term. By comparing the case without damping term as shown in Fig. 13, the resonance point at low frequency in the HVDC rectifier can be effectively removed by reshaping the impedance and the HVDC rectifier impedance does not intersect the impedance of the wind power inverter at any frequency lower than 100 Hz. The remaining resonance point in the HVDC converter is resulting from the LCL-filter.

Fig. 23 shows the Nyquist plot of the impedance ratio of the interconnected system. As can be seen, neither the d-axis nor the q-axis input impedance ratio of the HVDC rectifier and the wind power inverter encircle the point (-1, j0) which predicts the interconnected system will be stable.

The stability analysis discussed is performed for an equilibrium point with 100% wind power output. However, it might not be valid for other operating points; therefore, it is necessary to perform the stability analysis for all possible operating points. In this analysis, the stability analysis is performed for various operating points from 10%-100% wind power output power. Fig. 24 shows the Nyquist plot of the impedance ratio for two operating points at 40% and 100% wind power output with the active damping term for a case of comparison and the interconnected system is predicted to be stable for both

power levels.

To verify the theoretical analysis, a detailed simulation model of the interconnected system including the damping scheme in controller of the HVDC rectifier has been built. The control structure including the damping scheme is shown in Fig. 3. The active damping is implemented in such a way that it can remove all frequencies except around 50 Hz. The cut-off frequency of the low-pass filter is kept such that the output of the filter is only the dc components of the offshore ACC voltage. The active damping gain can be kept from 0 to 1. The system is investigated with the active damping for a damping gain of 0.5. The time domain simulations have been carried out for different operating points and the system is found to be stable for all operating points. The 3-phase instantaneous ac voltages and currents at ACC bus from time

domain simulation are shown in Fig. 25 (a) and the active and reactive power at ACC bus and the dc link voltage of the HVDC system are shown in Fig. 25 (b). From the time domain simulation it is clear that the system is stable as predicted by theoretical analysis in GNC plot of the impedance ratio (Fig. 23) and the proposed active damping scheme can effectively improve the oscillatory phenomena.

VI. DISCUSSION

Irrespective of the ability of the active damping to eliminate these oscillations, the understanding of the oscillatory phenomena at its source remain of crucial importance since they not only decrease the power quality and cause poor system performance but can greatly impact the stability of the overall interconnected system. Even if the active damping scheme has been effective in suppressing the oscillatory phenomena in the case presented in this paper, the various configurations and controllers in real life systems are not always known in the details due to confidentiality and industry secrecy. Therefore, further research efforts are needed in this field to better understand the implications of the different components and controllers in the manifestation of these oscillatory phenomena. It is often argued in the literature that controller interactions are the likely sources of these oscillations, but rigorous proofs of this claim have not been yet well reported. A very likely cause for this might simply be the lack of well established tools for analysing and proving interactions in multi-converter multi-controller power electronics systems. Among the tools available today and widely used in power systems research to analyse interactions between components and controllers of the system, the participation factor and sensitivity analysis tool is a good candidate. However, this tool will require a very detailed knowledge of every single parameter of the system under investigation.

Triggering the discussion on the need of such tools tailored for the complexity level of power electronics system and that can be less dependent on the very detailed knowledge of the system, is also one of the aims of this paper. As evidence coming from field experience shows more and more the criticality of this problem on systems similar to the one investigated in this paper, the scientific community in this field will see new methods and tools for the stability analysis of these systems emerging in the near future.

VII. CONCLUSION

This paper presented a preliminary exploration of the possible origins of the SSO and resonances observed in the interconnection of a wind farm and a VSC based HVDC system. The SSO and sub-harmonic resonance phenomena at low frequency is observed depending on the control implementation and components of the wind farm and the HVDC system. Analytical derivations of impedance frequency responses for both the wind farm and the HVDC were derived and potential resonance points were identified from the Nyquist plot of the impedance ratio. These resonance points are also observed in the form of oscillations in the time domain simulations of the wind farm and the HVDC with their spectral analysis.

A closer and step by step analysis of each component and controller of the wind farms and the HVDC indicates the possible sources for these oscillations. The SSO originated in the ac collection bus is arguably originated by the interaction between the WECS inverter controller and the HVDC rectifier. For testing the impact of controllers in mitigating the observed oscillations, this paper proposed an active damping scheme in the current compensator of the HVDC rectifier to improve such oscillation phenomena. The detailed analytical modeling of the damping scheme has been presented and the performance of the active damping scheme has been verified by time domain simulation. The oscillations are effectively eliminated with the active damping scheme.

APPENDIX

TABLE II: The VSC-HVDC system parameters

Parameter	Value	Parameter	Value
Rated Power, S_b	200 MVA	L_c	0.08 pu
Rated ac voltage	200 kV	R_c	0.003 pu
Rated frequecy	50 Hz	C_f	0.074 pu
Trans. inductance	0.15 pu	V_{dc}	400 kV
Trans. resistance	0.005 pu	L_{dc}/km	2.615mH
Grid inductance	0.0271 pu	R_{dc}/km	0.0011 Ω
Grid resistance	0.0191 pu	C_{dc}	4.4 pu

TABLE III: Parameter of ACC side WECS VSC

Parameter	Value	Parameter	Value
Rated Power, S_b	56 MW	$L_w f$	0.15 pu
Rated ac voltage	575 V	$R_w f$	0.15/50 pu
Rated dc voltage	1100 V	$C_w f$	0.0344 pu
Trans. inductance	0.04 pu	f	50 Hz
Trans. resistance	0.005 pu	C_{dc}	6.16 pu
L_{cable}/km	0.2526mH	R_{cable}/km	0.0843 Ω
C_{cable}/km	0.1837uF	Cable length	10 km

REFERENCES

[1] N. M. Kirby, L. Xu, M. Luckett and W. Siepmann, "HVDC transmission for large offshore wind farms," Power Engineering Journal, vol.16, no.3, pp.135,141, June 2002

[2] S. M. Muyeen, R. Takahashi and J. Tamura, "Operation and Control of HVDC-Connected Offshore Wind Farm," IEEE Transaction on Sustainable Energy, vol.1, no.1, pp.30,37, April 2010

[3] L. Xu, L. Yao and C. Sasse, "Grid Integration of Large DFIG-Based Wind Farms Using VSC Transmission," IEEE Transactions on Power Systems, vol.22, no.3, pp.976,984, Aug. 2007

[4] C. Li, P. Zhan, J. Wen, M, Yao, N. Li and W.-J. Lee, "Offshore Wind Farm Integration and Frequency Support Control Utilizing Hybrid Multiterminal HVDC Transmission," IEEE Transactions on Industry Applications, vol.50, no.4, pp.2788,2797, July-Aug. 2014

[5] X. Chen, H. Sun, J. Wen, W.-J. Lee, X. Yuan, N. Li and L. Yao, "Integrating Wind Farm to the Grid Using Hybrid Multiterminal HVDC Technology," IEEE Transactions on Industry Applications, vol.47, no.2, pp.965,972, March-April 2011

[6] W. Wang, A. Beddard, M. Barnes and O Marjanovic, "Analysis of Active Power Control for VSCHVDC," IEEE Transactions on Power Delivery, vol.29, no.4, pp.1978,1988, Aug. 2014

[7] C. Oates, "Modular Multilevel Converter Design for VSC HVDC Applications," IEEE Journal of Emerging and Selected Topics in Power Electronics, vol. 3, no. 2, pp. 505-515, June 2015.

[8] G.P. Adam and B.W. Williams, "Half- and Full-Bridge Modular Multilevel Converter Models for Simulations of Full-Scale HVDC Links and Multiterminal DC Grids," IEEE Journal of Emerging and Selected Topics in Power Electronics, vol.2, no.4, pp.1089,1108, Dec. 2014

[9] N. Flourentzou, V.G. Agelidis and G.D. Demetriades, "VSC-Based HVDC Power Transmission Systems: An Overview," IEEE Transactions on Power Electronics, vol.24, no.3, pp.592,602, March 2009

[10] J. Lv, P. Dong, G. Shi, X. Cai, H. Rao and J. Chen, "Subsynchronous oscillation of large DFIG-based wind farms integration through MMC-based HVDC," 2014 International Conference on Power System Technology (POWERCON), vol., no., pp.2401,2408, 20-22 Oct. 2014

[11] H. Liu and J. Sun, "Voltage Stability and Control of Offshore Wind Farms With AC Collection and HVDC Transmission," IEEE Journal of Emerging and Selected Topics in Power Electronics, vol.2, no.4, pp.1181,1189, Dec. 2014

[12] M. Bradt, B. Badrzadeh, E. Camm, D. Mueller, J. Schoene, T. Siebert, T. Smith, M. Starke, and R. Walling, R., "Harmonics and resonance issues in wind power plants," 2011 IEEE Power and Energy Society General Meeting, pp.1,8, 24-29 July 2011

[13] K.N.B.M. Hasan, K. Rauma, A. Luna, J.I. Candela and P. Rodriguez, "Harmonic Compensation Analysis in Offshore Wind Power Plants Using Hybrid Filters," IEEE Transactions on Industry Applications, vol.50, no.3, pp.2050,2060, May-June 2014

[14] L. Wang, X. Xie, Q. Jiang, H. Liu, Y. Li and H. Liu, "Investigation of SSR in Practical DFIG-Based Wind Farms Connected to a Series-Compensated Power System," in IEEE Transactions on Power Systems, vol. 30, no. 5, pp. 2772-2779, Sept. 2015.

[15] L. Harnefors, "Analysis of Subsynchronous Torsional Interaction With Power Electronic Converters," IEEE Transactions on Power Systems, vol.22, no.1, pp.305,313, Feb. 2007

[16] N. Prabhu and K.R. Padiyar "Investigation of Subsynchronous Resonance With VSC-Based HVDC Transmission Systems," IEEE Transactions on Power Delivery, vol.24, no.1, pp.433,440, Jan. 2009

[17] M. Cespedes and J. Sun, "Modeling and mitigation of harmonic resonance between wind turbines and the grid," 2011 IEEE Energy Conversion Congress and Exposition (ECCE), pp.2109,2116, 17-22 Sept. 2011

[18] M. Amin, J. Lv and M. Molinas, "Oscillatory Phenomena between Wind Farms and HVDC Systems: The impact of Control", 2015 IEEE 16th Workshop on Control and Modeling for Power Electronics (COMPEL), Vancouver, BC, 2015, pp. 1-8. 2015

[19] R.K. Varma, S. Auddy and Y. Semsedini, "Mitigation of Subsynchronous Resonance in a Series-Compensated Wind Farm Using FACTS Controllers," IEEE Transactions on Power Delivery, vol.23, no.3, pp.1645,1654, July 2008

[20] L. Fan and Z. Miao, "Mitigating SSR Using DFIG-Based Wind Generation," IEEE Transactions on Sustainable Energy, vol.3, no.3, pp.349,358, July 2012

[21] Q. Wang and L. Chang, "An intelligent maximum power extraction algorithm for inverter-based variable speed wind turbine systems," IEEE Transactions on Power Electronics, vol.19, no.5, pp.1242-1249, Sept. 2004

[22] J. Sun, "Impedance-Based Stability Criterion for Grid-Connected Inverters," IEEE Transactions on Power Electronics, vol.26, no.11, pp.3075-3078, Nov. 2011

[23] B. Wen, D. Dong, D. Boroyevich, R. Burgos, P. Mattavelli and Z. Shen, "Impedance-Based Analysis of Grid-Synchronization Stability for Three-Phase Paralleled Converters," IEEE Transactions on Power Electronics, vol.31, no.1, pp.26-38, Jan. 2016

[24] M. Amin; M. Molinas; J. Lyu; X. Cai, "Impact of Power Flow Direction on the Stability of VSC-HVDC Seen from the Impedances Nyquist Plot," in IEEE Transactions on Power Electronics , vol.PP, no.99, 2016

[25] M. Amin, A. Rygg and M. Molinas, Impedance-based and Eigenvalue based Stability Assessment Compared in VSC-HVDC System, In 8th Annual IEEE Energy Conversion Congress & Exposition (ECCE 2016), Milwaukee, USA 2016

[26] B. Wen, D. Boroyevich, R. Burgos, P. Mattavelli, and Z. Shen, Analysis of D-Q small-signal impedance of grid-tied inverters, IEEE Trans. on Power Electronics, vol. 31, no. 1, pp. 675-687, January 2016.

[27] B. Wen, D. Boroyevich, R. Burgos, P. Mattavelli, and Z. Shen, "Small-Signal Stability Analysis of Three-Phase AC Systems in the Presence of Constant Power Loads Based on Measured d-q Frame Impedances," IEEE Transactions on Power Electronics, vol.30, no.10, pp.5952-5963, Oct. 2015

[28] R. D. Middlebrook "Input filter considerations in design and application of switching regulators" Rec.1976 IEEE Ind. Appl. Soc. Annu. Meeting, pp. 366-382,

[29] V. Blasko, and V. Kaura, "A new mathematical model and control of a three-phase AC-DC voltage source converter," IEEE Transactions on Power Electronics, vol.12, no.1, pp.116,123, Jan 1997

[30] N. Kroutikova, C.A. Hernandez-Aramburo, and T.C. Green, "State-space model of grid-connected inverters under current control mode," IET Electric Power Applications, vol.1, no.3, pp.329,338, May 2007

[31] C. Bajracharya, M. Molinas, J. A. Suul, and T. Undeland, "Understanding of tuning techniques of converter controllers for VSC-HVDC," in Proceedings of NORPIE 2008, Helsinki, Finland, 09-11 June 2008

[32] N.W. Miller, J.J. Sanchez-Gasca, W.W. Price, and R.W. Delmerico, "Dynamic modeling of GE 1.5 and 3.6 MW wind turbine-generators for stability simulations," in IEEE Power Engineering Society General Meeting, pp.1977-1983 13-17 July 2003

[33] V. Kaura, and V. Blasko, "Operation of a phase locked loop system under distorted utility conditions," IEEE Transactions on Industry Applications, vol.33, no.1, pp.58,63, Jan/Feb 1997

[34] R. Ottersten, On control of back-to-back converters and sensor-less induction machine drives, Ph.D. dissertation, Dept. Elect. Power Eng., Chalmers Univ. Technol., Gteborg, Sweden, 2003.

[35] L. Harnefors, M. Bongiorno and S. Lundberg, "Input-Admittance Calculation and Shaping for Controlled Voltage-Source Converters," in IEEE Transactions on Industrial Electronics, vol. 54, no. 6, pp. 3323-3334, Dec. 2007.

[36] S. Shah and L. Parsa, "Sequence Domain Transfer Matrix Model of Three-Phase Voltage Source Converters" in Proc. of Power and Energy Society Gen. Meeting, 2016.

[37] A. Rygg, M. Molinas, Z. Chen and X. cai, "A modified sequence domain impedance definition and its equivalence to the dq-domain impedance definition for the stability analysis of AC power electronic systems," in IEEE Journal of Emerging and Selected Topics in Power Electronics , vol.PP, no.99, pp.1-1, 2016

[38] R. Burgos, D. Boroyevich, F. Wang, K. Karimi, and G. Francis, On the ac stability of high power factor three-phase rectifiers, in Proc. Energy Convers. Congr. Expo., Sep. 2010, pp. 20472054.

[39] B. Wen, D. Boroyevich, P. Mattavelli, R. Burgos, and Z. Shen, D-Q impedance specification for balanced three-phase ac distributed power system, in Proc. 30th Annu. Appl. Power Electron. Conf. Expo., Mar. 2015.

[40] H. H. Rosenbrock, Computer-Aided Control System Design. NY: Academic Press, 1974, pp. 142-149.

Mohammad Amin (M'11) received the B.Sc. degree in electrical and electronic engineering from Chittagong University of Engineering and Technology, Chittagong, Bangladesh, and the M.Sc. degree in electric power engineering from Chalmers University of Technology, Gothenburg, Sweden in 2008 and 2011, respectively. He is working toward the Ph.D. degree at Norwegian University of Science and Technology, Trondheim, Norway.

He was with the Department of Electrical and Electronic Engineering, International Islamic University Chittagong as an Assistant Professor from December 2011 to July 2013. He was a Ph.D. Visiting Scholar at the Wind Power Research Center, Shanghai Jiao Tong University, Shanghai, China, from May 2015 to July 2015. His research interests include stability and interaction analysis in voltage-source-converter- and modular-multilevel-converter-based offshore high-voltage dc system, grid integration of wind farm, control of power converters, and flexible ac transmission systems.

Marta Molinas (M'94) received the Diploma degree in electromechanical engineering from the National University of Asuncion, Asuncion, Paraguay, in 1992; the Master of Engineering degree from Ryukyu University, Japan, in 1997; and the Doctor of Engineering degree from the Tokyo Institute of Technology, Tokyo, Japan, in 2000. She was a Guest Researcher with the University of Padova, Padova, Italy, during 1998. From 2004 to 2007, she was a Postdoctoral Researcher with the Norwegian University of Science and Technology (NTNU) and from 2008-2014 she has been professor at the Department of Electric Power Engineering at the same university. She is currently Professor at the Department of Engineering Cybernetics, NTNU. Her research interests include stability of power electronics systems, harmonics, instantaneous frequency, and non-stationary signals from the human and the machine. She is Associate Editor for the IEEE Journal JESTPE, IEEE PELS Transactions and Editor of the IEEE Transactions on Energy Conversion. Dr. Molinas has been an AdCom Member of the IEEE Power Electronics Society from 2009 to 2011.